SCIENCE CHINA Materials **ARTICLES**

mater.scichina.com link.springer.com Published online 15 January 2018 | https://doi.org/10.1007/s40843-017-9171-9
Sci China Mater 2018, 61(6): 861–868

SPECIAL ISSUE: Advanced Materials for Photoelectrochemical Cells

Novel Cu_3P/g-C_3N_4 p-n heterojunction photocatalysts for solar hydrogen generation

Zhixiao Qin, Menglong Wang, Rui Li and Yubin Chen*

ABSTRACT Developing efficient heterostructured photocatalysts to accelerate charge separation and transfer is crucial to improving photocatalytic hydrogen generation using solar energy. Herein, we report for the first time that p-type copper phosphide (Cu_3P) coupled with n-type graphitic carbon nitride (g-C_3N_4) forms a p-n junction to accelerate charge separation and transfer for enhanced photocatalytic activity. The optimized Cu_3P/g-C_3N_4 p-n heterojunction photocatalyst exhibits 95 times higher activity than bare g-C_3N_4, with an apparent quantum efficiency of 2.6% at 420 nm. A detail analysis of the reaction mechanism by photoluminescence, surface photovoltaics and electrochemical measurements revealed that the improved photocatalytic activity can be ascribed to efficient separation of photo-induced charge carriers. This work demonstrates that p-n junction structure is a useful strategy for developing efficient heterostructured photocatalysts.

Keywords: photocatalysis, copper phosphide, p-n junction, heterostructure, hydrogen production

INTRODUCTION

Hydrogen is considered to be an ideal energy source to substitute fossil fuel due to its high energy capacity and environmental friendliness [1]. Since the discovery of the Honda-Fujishima effect in 1972 [2], photocatalytic hydrogen production from water has attracted much attention as an ideal solution to global energy and environmental issues [3–6]. Developing highly active, long-term stable and low-cost photocatalysts is still a key to their commercial application. Recently, graphitic carbon nitride (g-C_3N_4) has emerged as an attractive metal-free polymeric semiconductor for photocatalytic hydrogen generation due to its specific laminar structure, high stability and capability of visible-light harvest [7–11]. However, the severe photo-induced charge recombination and surface reaction still restrict the photocatalytic performance. Loading suitable cocatalysts seems to be a useful approach to boost photocatalytic hydrogen generation [12–14]. To date, Pt has been widely utilized as an efficient cocatalyst with g-C_3N_4, leading to significantly improved performances [15]. However, the high cost and low reserve of Pt limit the large-scale application and hence the development of non-precious photocatalytic system is quite appealing.

Recently, it has been demonstrated that a series of transition-metal phosphides could promote the photocatalytic hydrogen generation superior to g-C_3N_4 as cocatalysts [16–19]. For instance, our previous work demonstrated that Ni_2P cocatalyst could significantly increase photocatalytic performance for hydrogen generation over g-C_3N_4 [16]. Jiang *et al.* [17] reported that CoP was also an efficient cocatalyst to enhance the photocatalytic activity of g-C_3N_4. Besides g-C_3N_4, the photocatalytic properties of various semiconductor photocatalysts such as CdS [20–22], TiO_2 [16,23], and $Cd_xZn_{1-x}S$ [24] could also be increased by coupling with transition-metal phosphides. However, the reported reaction mechanisms of these transition-metal phosphides are quite different. It is necessary to investigate more general coupling principle between photocatalysts and transition-metal phosphides as a guidance to develop efficient noble-metal-free hybrid photocatalysts.

Coupling semiconductors with different band structures to form heterojunction structure has been proved to be an effective way to promote the charge separation and photocatalytic performance [24–26]. When p-type semiconductor is combined with n-type semiconductor, a

International Research Center for Renewable Energy, State Key Laboratory of Multiphase Flow in Power Engineering, Xi'an Jiaotong University, Xi'an 710049, China
* Corresponding author (email: ybchen@mail.xjtu.edu.cn)

built-in electric field is achieved across the p-n junction region, which can efficiently promote the separation of photo-induced charges [27]. Copper phosphide (Cu_3P) is a p-type semiconductor with a band gap of 1.5 eV [23]. Due to its low cost and earth-abundant elements, Cu_3P was previously reported for application in lithium ion batteries [28–30]. However, the utilization of Cu_3P in photocatalytic hydrogen generation is still limited. Herein, we report a novel and low-cost Cu_3P/g-C_3N_4 p-n heterojunction photocatalyst for highly efficient hydrogen generation. Nanoscale p-n junctions developed in the hybrid photocatalysts could efficiently improve the photo-induced charge separation, leading to the significantly enhanced photocatalytic performance.

EXPERIMENTAL SECTION

Synthesis procedure

All chemicals in the present study are of analytical grade and used as received without further purification. g-C_3N_4 was synthesized by heating 10 g of urea at 550°C for 2 h in the air to obtain yellow powder. In a typical synthesis, $Cu(OH)_2$/g-C_3N_4 was prepared by a simple precipitation method. 0.4 g of g-C_3N_4 was dispersed in 100 mL of 0.25 mol L^{-1} NaOH aqueous solution, and then $Cu(NO_3)_2 \cdot 3H_2O$ was added under stirring. The mixed solution was stirred for 6 h at room temperature. The products were collected and washed three times with deionized water and ethanol. Then the precipitates were dried in a vacuum oven at 80°C for 5 h. Finally, Cu_3P/g-C_3N_4 photocatalyst was synthesized through a solid-state reaction. Typically, 0.2 g of the prepared $Cu(OH)_2$/g-C_3N_4 and 0.1 g of NaH_2PO_2 were blended mechanically and ground into fine power. Then, the fine power was annealed at 300°C for 2 h in a quartz tube with a heating rate of 5 °C min^{-1} under Ar flow. The obtained products were washed with deionized water to remove residual salts, and dried under vacuum at 50°C. The Cu_3P was also prepared using a similar procedure. The loading weight of Cu_3P in Cu_3P/g-C_3N_4 was measured by X-ray photoelectron spectroscopy (XPS) analysis and the results were shown in Table S1. The practical loading concentrations of Cu_3P were close to the theoretical values.

Characterization

X-ray powder diffraction (XRD) patterns were obtained from a PANalytical X'pert MPD Pro X-ray diffractometer. Transmission electron microscopy (TEM) images were obtained using a FEI Tecnai G2 F30 S-Twin microscope attached with an OXFORD MAX-80 energy dispersive X-ray (EDX) system. UV-visible (UV-vis) absorption spectra were measured on a HITACHI U4100 spectrophotometer. XPS measurements were conducted on a Kratos Axis-Ultra multifunctional X-ray spectrometer. All binding energies were referenced to the C 1s peak at 284.8 eV. Photoluminescence (PL) spectra were examined using a PTI QM-4 fluorescence spectrophotometer with an excitation wavelength of 320 nm. The lock-in-based surface photovoltage (SPV) spectra were obtained using a surface photovoltage spectroscope. The measurement system consists of a source of monochromatic light (Omni-λ300), a lock-in amplifier (SR830) with a light chopper (SR540), and a sample chamber.

Visible-light-driven photocatalytic measurement

Photocatalytic hydrogen generation was performed in a side irradiation Pyrex cell with a magnetic stirring. Typically, 20 mg of the as-prepared photocatalyst was added into 80 mL of aqueous solution containing 10 vol% triethanolamine (TEOA) as the electron donors. Before irradiation, nitrogen was purged into the reaction cell for 30 min to remove air in the dark. The reaction temperature was kept at 35°C. A 300 W Xe-lamp equipped with a 420 nm cutoff filter was employed to provide the visible-light irradiation. The amount of generated hydrogen was measured by gas chromatography using a thermal conductivity detector (TCD). The apparent quantum efficiency (AQE) could be calculated as AQE(%) =(the number of evolved hydrogen molecules×2/the number of incident photons)×100%.

RESULTS AND DISCUSSION

Physicochemical properties of Cu_3P/g-C_3N_4 heterostructure

The crystal structures of the as-prepared samples were investigated by XRD. As shown in Fig. 1, two distinct diffraction peaks of bare g-C_3N_4 could be attributed to the graphitic phase with tri-s-triazine units. The Cu_3P sample shows diffraction peaks located at 36.0°, 39.0°, 41.5°, 45.1°, and 46.2°, corresponding to the (112), (202), (211), (300), and (213) planes of hexagonal Cu_3P (PDF#71-2261) [22]. It has been reported that trace amount of Cu was involved in the Cu_3P sample, which was prepared *via* a phosphatization method [23]. The main diffraction peaks of Cu_3P/g-C_3N_4 could be attributed to the graphitic phase g-C_3N_4. There were not apparent peaks corresponding to Cu_3P, possibly due to the low amount and high dispersity.

We further investigated the morphology of g-C_3N_4 photocatalysts after loading Cu_3P. As displayed in Fig. 2a,

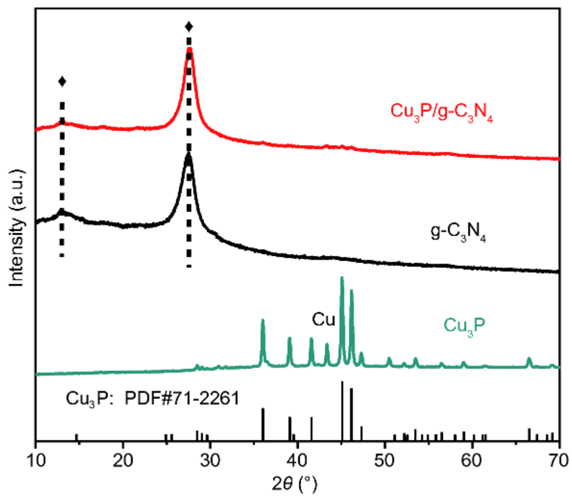

Figure 1 XRD patterns of Cu_3P, $g-C_3N_4$, and $Cu_3P/g-C_3N_4$.

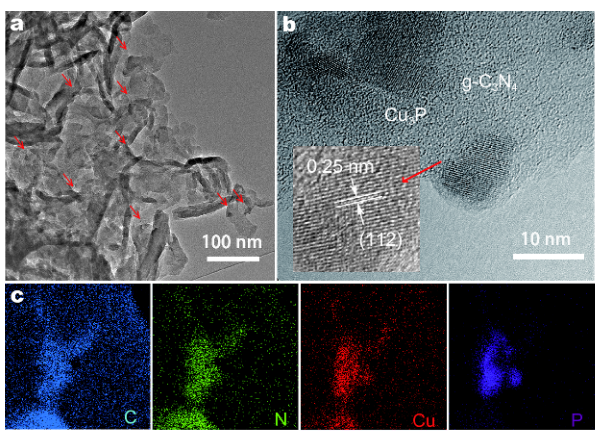

Figure 2 (a) TEM and (b) HRTEM images of $Cu_3P/g-C_3N_4$. (c) Elemental mapping of C, N, Cu, and P species in $Cu_3P/g-C_3N_4$ (excess C and Cu signals came from the carbon film on the copper grid).

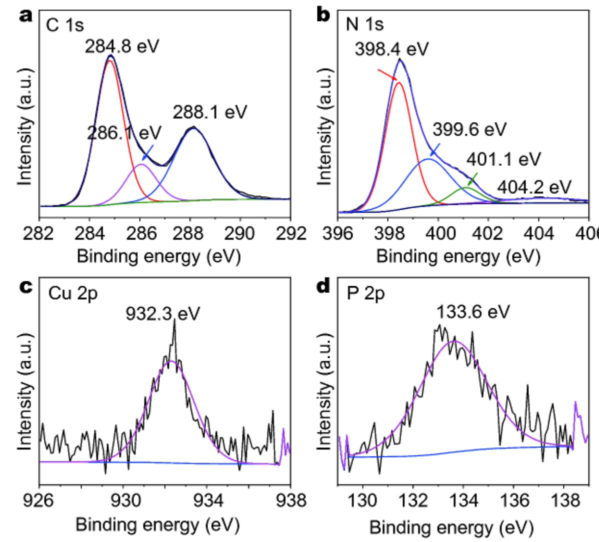

Figure 3 XPS spectra of $Cu_3P/g-C_3N_4$. (a) C 1s, (b) N 1s, (c) Cu 2p, and (d) P 2p.

the hybrid samples had uniformly dispersed Cu_3P nanoparticles anchored on the surface of $g-C_3N_4$ nanosheets (Fig. 2b). The lattice distance of 0.25 nm corresponded to the (112) plane of hexagonal Cu_3P. To determine the composition and element distribution of $Cu_3P/g-C_3N_4$, the elemental mapping of C, N, Cu, and P species was carried out (Fig. 2c). It was proved that Cu_3P nanoparticles were successfully distributed on the surface of $g-C_3N_4$. The specific surface area of $Cu_3P/g-C_3N_4$ was 70.2 $m^2\ g^{-1}$, which was close to that of single $g-C_3N_4$ (73.1 $m^2\ g^{-1}$). This result indicated that the fabrication of hybrid samples did not lead to agglomeration of $g-C_3N_4$.

XPS measurements were performed to investigate the surface chemical states of $Cu_3P/g-C_3N_4$. As shown in Fig. 3a, the typical values for C–C, C–NH_2, and N–C=N in $g-C_3N_4$ were respectively presented at binding energies of 284.8, 286.1, and 288.1 eV [31]. Meanwhile, the peaks at 398.4, 399.6, 401.1, and 404.2 eV of N 1s spectrum (Fig. 3b) could be assigned to the binding energies of C–N=C, N–$(C)_3$, C–N–H, and π excitations of $g-C_3N_4$, respectively [24]. Fig. 3c shows the Cu 2p profile with a peak located at 932.3 eV, and the P 2p region has a single peak at 133.6 eV (Fig. 3d). The peak at 932.3 eV could be ascribed to Cu–P in Cu_3P, and the peak at 133.6 eV arose from oxidized P species probably due to the air exposure [23]. The XPS results further demonstrated the successful synthesis of Cu_3P and $g-C_3N_4$ in the heterostructure.

The optical properties of the as-prepared samples were measured by UV-vis spectrophotometer. As shown in Fig. 4a, the spectrum of bare $g-C_3N_4$ displayed a sharp edge at around 450 nm. After the coupling of Cu_3P onto the $g-C_3N_4$ surface, an increased absorption in visible range of 400–800 nm was observed. Meanwhile, the UV-vis absorption spectrum of pure Cu_3P (Fig. 4b) showed an apparent absorption from 300 to 800 nm. The absorption peak around 550 nm could be attributed to the plasmon peak of Cu nanoparticles in as-prepared Cu_3P sample [32]. The optical band gaps (E_g) of $g-C_3N_4$ and Cu_3P were estimated from Tauc plots of $(\alpha h\nu)^n$ *vs.* photon energy ($h\nu$) [33]. The insets show that the band gaps of $g-C_3N_4$ and Cu_3P were respectively determined to be 2.72 and 1.50 eV, which were consistent with the previous studies [23,34].

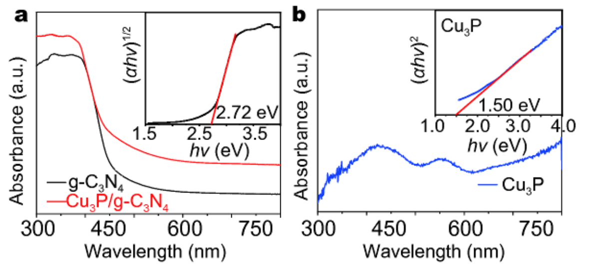

Figure 4 UV-vis absorption spectra of (a) g-C_3N_4, Cu_3P/g-C_3N_4 and (b) Cu_3P. The insets show the plots of $(\alpha h\nu)^{1/2}$ *vs.* photon energy ($h\nu$) for g-C_3N_4 and $(\alpha h\nu)^2$ *vs.* $h\nu$ for Cu_3P.

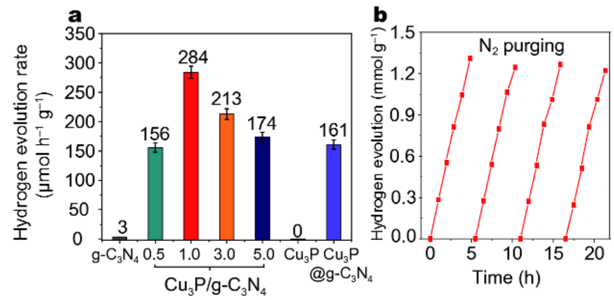

Figure 5 (a) Photocatalytic hydrogen evolution rates of g-C_3N_4, Cu_3P/g-C_3N_4 (the loading amount of Cu_3P was respectively 0.5, 1, 3, and 5 wt%), Cu_3P, and physically mixed Cu_3P@g-C_3N_4 (the loading amount of Cu_3P was 1 wt%). (b) Long-time photocatalytic test of 1 wt% Cu_3P/g-C_3N_4 sample for hydrogen evolution. (Reaction condition: 20 mg of photocatalysts, 80 mL of aqueous solution containing 10 vol% TEOA, 300 W Xe lamp equipped with a cutoff filter ($\lambda \geq 420$ nm).

Photocatalytic hydrogen production

The photocatalytic hydrogen generation was subsequently investigated in triethanolamine (TEOA) aqueous solution under visible-light irradiation. As shown in Fig. 5a, the hydrogen production rate of bare g-C_3N_4 was rather low, and Cu_3P could significantly boost the photocatalytic hydrogen generation of g-C_3N_4. The rate of hydrogen generation initially increased and then decreased with increasing amount of Cu_3P. With the optimal loading amount of Cu_3P, Cu_3P/g-C_3N_4 showed the highest hydrogen production rate of 284 μmol h^{-1} g^{-1}, which was about 95 times higher than that of bare g-C_3N_4. The apparent quantum efficiency (AQE) for hydrogen generation was calculated to be 2.6% at 420 nm. However, no appreciable hydrogen generation could be detected in bare Cu_3P, indicating that Cu_3P was not an active photocatalyst [22]. By comparison, the activity of physically mixed Cu_3P@g-C_3N_4 was measured under the same condition. The hydrogen production rate of Cu_3P@g-C_3N_4 was much lower than that of Cu_3P/g-C_3N_4, revealing that the intimate contact between Cu_3P and g-C_3N_4 takes effect on the performance [24]. Long-term photocatalytic test of Cu_3P/g-C_3N_4 for hydrogen generation was carried out to evaluate the stability of Cu_3P/g-C_3N_4 hybrid photocatalysts. As displayed in Fig. 5b, there was no apparent decrease in the photocatalytic activity over the 20 h reaction, indicating its good stability.

Mechanism study

PL spectra of the as-prepared samples were measured to explore the charge separation and migration behaviors in the photocatalyst. As shown in Fig. 6a, both g-C_3N_4 and Cu_3P/g-C_3N_4 exhibited broad emission peaks centered around 450 nm, corresponding to the band gap of g-C_3N_4. Compared to pure g-C_3N_4, Cu_3P/g-C_3N_4 showed apparently decreased PL intensity, which indicated that loading Cu_3P could facilitate the charge transfer so as to inhibit the charge recombination in g-C_3N_4 [35], which was beneficial to photocatalytic performance.

The lock-in-based SPV spectra were also carried out to reveal the transfer properties of the photo-induced charge carriers. The signal of SPV can be attributed to the variation of surface potential barriers during the light irradiation, which can identify the light-responsive wavelength range and the separation efficiency of the electron-hole pairs in the photocatalysts [36]. As shown in Fig. 6b, positive photovoltaic responses ranging from 300 to 400 nm were observed for g-C_3N_4, indicating that g-C_3N_4 is a typical n-type semiconductor [37]. After loading Cu_3P on the surface of g-C_3N_4, the response signal of Cu_3P/g-C_3N_4 was obviously enhanced. The enhanced SPV signal intensity indicated that the introduction of Cu_3P was beneficial to the photo-induced charge separation in Cu_3P/g-C_3N_4 heterostructures [38].

In addition to the charge-transfer behavior in the photocatalyst, the charge-transfer at the photocatalyst/solution interface is also crucial to the photocatalytic performance. Therefore, g-C_3N_4 and Cu_3P/g-C_3N_4 electrodes were fabricated (see Supplementary information) and the electrochemical impedance spectroscopy (EIS) was performed to elucidate the charge-transfer resistances. As shown in Fig. 7a, the Nyquist impedance plots for the electrodes could be fitted to an equivalent circuit (the inset) consisting of the series resistance (R_s), charge transfer resistance from the electrode to the electrolyte (R_{ct}), recombination resistance at the electrode interface (R_{rec}), and constant phase elements (CPE1 and CPE2). As summarized in Table S2, the values of R_{ct} and R_{rec} for Cu_3P/g-C_3N_4 were lower than those of g-C_3N_4, indicating that the Cu_3P/g-C_3N_4 had efficient charge-

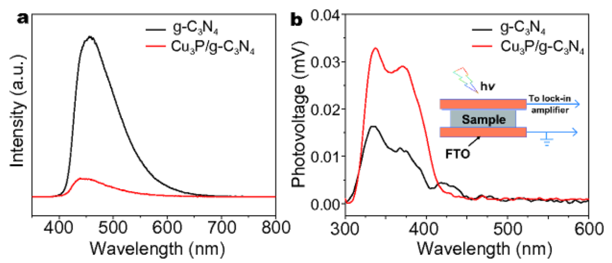

Figure 6 (a) PL spectra of g-C_3N_4 and Cu_3P/g-C_3N_4. (b) SPV spectra of g-C_3N_4 and Cu_3P/g-C_3N_4. The inset shows the schematic setup for the SPV measurement.

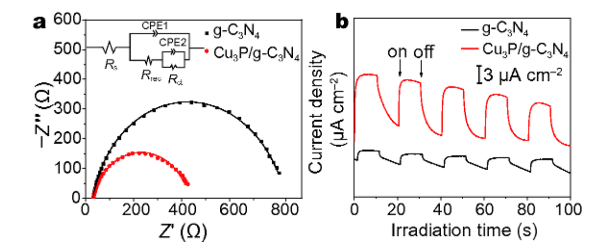

Figure 7 (a) Nyquist impedance plots of g-C_3N_4 and Cu_3P/g-C_3N_4 measured at −1.0 V *vs.* RHE in N_2-saturated 0.5 mol L^{-1} Na_2SO_4 aqueous solution. The inset shows the equivalent circuit. (b) Transient photocurrent responses of g-C_3N_4 and Cu_3P/g-C_3N_4 measured at 0.2V *vs.* RHE in N_2-saturated 0.5 mol L^{-1} Na_2SO_4 aqueous solution. A 500 W Xe lamp coupled with an AM 1.5 filter was used as the light source for the photocurrent measurement.

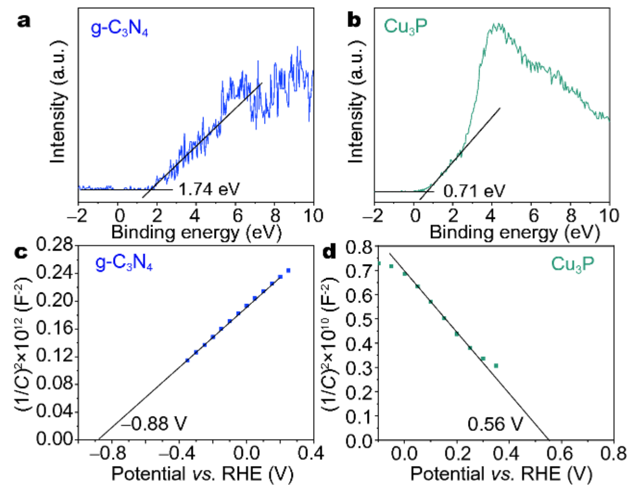

Figure 8 XPS valence band spectra for (a) g-C_3N_4 and (b) Cu_3P. Mott-Schottky plots of (c) g-C_3N_4 and (d) Cu_3P in N_2-saturated 0.5 mol L^{-1} Na_2SO_4 aqueous solution.

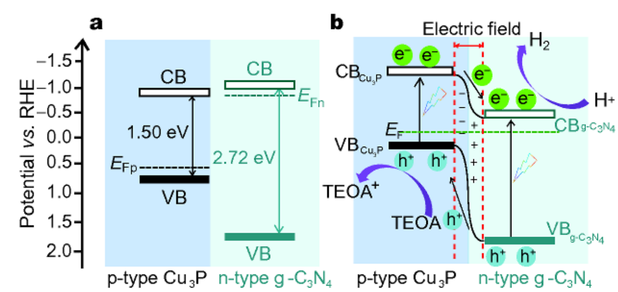

Figure 9 (a) Energy band structures of Cu_3P and g-C_3N_4 before formation of the heterojunction. (b) The band structure for Cu_3P/g-C_3N_4 heterojunction and charge separation process under illumination.

transfer behavior at the photocatalyst/solution interface [16,39]. The transient photocurrent responses of g-C_3N_4 and Cu_3P/g-C_3N_4 were also investigated to examine their photoelectrochemical properties. As shown in Fig. 7b, Cu_3P/g-C_3N_4 exhibited a much higher photocurrent density than that of pure g-C_3N_4, suggesting a noticeable improvement in the suppression of charge recombination [40], which was consistent with PL and SPV results.

The spectroscopic and electrochemical analyses revealed that Cu_3P/g-C_3N_4 owns efficient charge separation, which is essential to achieve high photocatalytic activity. To better understand the photo-induced charge carrier dynamics involved in the Cu_3P/g-C_3N_4 heterojunction, the band alignment of Cu_3P and g-C_3N_4 were investigated. The valence band positions (E_{VB}) of Cu_3P and g-C_3N_4 were firstly measured by XPS valence band spectra. As displayed in Fig. 8a, b, the E_{VB} of Cu_3P and g-C_3N_4 were determined to be 0.71 and 1.74 eV, respectively. Since the band gaps (E_g) of Cu_3P and g-C_3N_4 were 1.50 and 2.72 eV, respectively, the conduction band positions (E_{CB}) of Cu_3P and g-C_3N_4 were calculated to be −0.79 and −0.98 eV, according to the equation: $E_{VB} = E_{CB} + E_g$ [41]. Mott-Schottky plot of g-C_3N_4 showed (Fig. 8c) a positive slope, indicating that it is an n-type semiconductor, while a negative slope of Cu_3P (Fig. 8d) corresponds to a p-type semiconductor [42]. The flat-band potentials of Cu_3P and g-C_3N_4 were estimated to be 0.56 and −0.88 V *vs.* RHE, which were close to the determined E_{VB} of Cu_3P and E_{CB} of g-C_3N_4. As shown in Fig. S1, Cu_3P/g-C_3N_4 exhibited the similar feature as pristine g-C_3N_4 owing to the low amount of Cu_3P. A positive slope was observed for Cu_3P/g-C_3N_4, and the flat band potential was determined to be −0.75 V *vs.* RHE, which was close to that of g-C_3N_4.

Therefore, the energy band structures of Cu_3P and g-C_3N_4 before forming the heterojunction are shown in Fig. 9a. The Fermi level (E_F) of g-C_3N_4 is higher than that of Cu_3P. When p-type Cu_3P is coupled with n-type g-C_3N_4, electrons will transfer from g-C_3N_4 to Cu_3P until the Fermi levels to be equal for both phases [43]. As shown in Fig. 9b, a built-in electric field is formed across the p-n junction, where the p-type Cu_3P region is negatively charged, and the n-type g-C_3N_4 region is positively charged. When Cu_3P/g-C_3N_4 photocatalysts are irradiated with visible light, the photo-induced electrons and holes will be obtained in Cu_3P and g-C_3N_4. As a result of the built-in electric field, the photo-induced electrons in the CB of Cu_3P will diffuse into the CB of g-C_3N_4 through the p-n junction, giving rise to the accumulation of photo-induced electrons in g-C_3N_4. Meanwhile, the photo-induced holes in the VB of g-C_3N_4 will diffuse into the VB of Cu_3P, leading to the accumulation of photo-induced holes in Cu_3P. Subsequently, the accumulated photo-induced electrons can transfer to the surface of g-C_3N_4 to reduce H^+ for hydrogen production, and the accumulated photo-induced holes can migrate to the surface of Cu_3P to oxidize TEOA. As a consequence, the efficient charge separation is successfully achieved by the p-n junctions in hybrid Cu_3P/g-C_3N_4. During the photocatalytic reaction, Cu_3P captured the photo-induced holes in g-C_3N_4 and functioned as the active sites for the surface oxidation reaction.

CONCLUSIONS

In summary, Cu_3P/g-C_3N_4 heterostructures were successfully constructed to achieve the efficient separation of photo-induced charges. Cu_3P nanoparticles were tightly attached to the surface of g-C_3N_4, leading to the formation of p-n junctions between p-type Cu_3P and n-type g-C_3N_4. The p-n junctions could promote charge transfer and reduce charge recombination, leading to an enhanced photocatalytic activity. The optimized Cu_3P/g-C_3N_4 p-n heterojunction photocatalyst exhibits 95 times higher activity than bare g-C_3N_4, with an apparent quantum efficiency of 2.6% at 420 nm. This work proposes an effective guidance to develop efficient noble-metal-free hybrid photocatalysts by p-n junction structure.

Received 30 October 2017; accepted 28 November 2017; published online 15 January 2018

1 Gray HB. Powering the planet with solar fuel. Nat Chem, 2009, 1: 7
2 Fujishima A, Honda K. Electrochemical photolysis of water at a semiconductor electrode. Nature, 1972, 238: 37–38
3 Chen X, Shen S, Guo L, *et al.* Semiconductor-based photocatalytic hydrogen generation. Chem Rev, 2010, 110: 6503–6570
4 Tong H, Ouyang S, Bi Y, *et al.* Nano-photocatalytic materials: possibilities and challenges. Adv Mater, 2012, 24: 229–251
5 Zhang K, Guo L. Metal sulphide semiconductors for photocatalytic hydrogen production. Catal Sci Technol, 2013, 3: 1672–1690
6 Su J, Zhou J, Wang L, *et al.* Synthesis and application of transition metal phosphides as electrocatalyst for water splitting. Sci Bull, 2017, 62: 633–644
7 Wang X, Maeda K, Thomas A, *et al.* A metal-free polymeric photocatalyst for hydrogen production from water under visible light. Nat Mater, 2009, 8: 76–80
8 Liu G, Wang T, Zhang H, *et al.* Nature-inspired environmental "phosphorylation" boosts photocatalytic H_2 production over carbon nitride nanosheets under visible-light irradiation. Angew Chem, 2015, 127: 13765–13769
9 Liu J, Liu Y, Liu N, *et al.* Metal-free efficient photocatalyst for stable visible water splitting *via* a two-electron pathway. Science, 2015, 347: 970–974
10 Li Y, Xu H, Ouyang S, *et al. In situ* surface alkalinized g-C_3N_4 toward enhancement of photocatalytic H_2 evolution under visible-light irradiation. J Mater Chem A, 2016, 4: 2943–2950
11 Ong WJ, Tan LL, Ng YH, *et al.* Graphitic carbon nitride (g-C_3N_4)-based photocatalysts for artificial photosynthesis and environmental remediation: are we a step closer to achieving sustainability? Chem Rev, 2016, 116: 7159–7329
12 Qin Z, Chen Y, Wang X, *et al.* Intergrowth of cocatalysts with host photocatalysts for improved solar-to-hydrogen conversion. ACS Appl Mater Interfaces, 2016, 8: 1264–1272
13 Chang K, Mei Z, Wang T, *et al.* MoS_2/Graphene cocatalyst for efficient photocatalytic H_2 evolution under visible light irradiation. ACS Nano, 2014, 8: 7078–7087
14 Yang J, Wang D, Han H, *et al.* Roles of cocatalysts in photocatalysis and photoelectrocatalysis. Acc Chem Res, 2013, 46: 1900–1909
15 Maeda K, Wang X, Nishihara Y, *et al.* Photocatalytic activities of graphitic carbon nitride powder for water reduction and oxidation under visible light. J Phys Chem C, 2009, 113: 4940–4947
16 Chen Y, Qin Z. General applicability of nanocrystalline Ni_2P as a noble-metal-free cocatalyst to boost photocatalytic hydrogen generation. Catal Sci Technol, 2016, 6: 8212–8221
17 Yi SS, Yan JM, Wulan BR, *et al.* Noble-metal-free cobalt phosphide modified carbon nitride: an efficient photocatalyst for hydrogen generation. Appl Catal B-Environ, 2017, 200: 477–483
18 Indra A, Acharjya A, Menezes PW, *et al.* Boosting visible-light-driven photocatalytic hydrogen evolution with an integrated nickel phosphide-carbon nitride system. Angew Chem Int Ed, 2017, 56: 1653–1657
19 Zhao H, Sun S, Jiang P, *et al.* Graphitic C_3N_4 modified by Ni_2P cocatalyst: an efficient, robust and low cost photocatalyst for visible-light-driven H_2 evolution from water. Chem Eng J, 2017, 315: 296–303
20 Sun Z, Zheng H, Li J, *et al.* Extraordinarily efficient photocatalytic hydrogen evolution in water using semiconductor nanorods integrated with crystalline Ni_2P cocatalysts. Energy Environ Sci, 2015, 8: 2668–2676
21 Cao S, Chen Y, Wang CJ, *et al.* Spectacular photocatalytic hydrogen evolution using metal-phosphide/CdS hybrid catalysts under sunlight irradiation. Chem Commun, 2015, 51: 8708–8711
22 Sun Z, Yue Q, Li J, *et al.* Copper phosphide modified cadmium sulfide nanorods as a novel p-n heterojunction for highly efficient visible-light-driven hydrogen production in water. J Mater Chem A, 2015, 3: 10243–10247
23 Yue X, Yi S, Wang R, *et al.* A novel and highly efficient earth-abundant Cu_3P with TiO_2 "P-N" heterojunction nanophotocatalyst for hydrogen evolution from water. Nanoscale, 2016, 8: 17516–17523
24 Qin Z, Xue F, Chen Y, *et al.* Spatial charge separation of one-dimensional Ni_2P-$Cd_{0.9}Zn_{0.1}S$/g-C_3N_4 heterostructure for high-quantum-yield photocatalytic hydrogen production. Appl Catal B-

Environ, 2017, 217: 551–559
25 Chen Y, Qin Z, Wang X, *et al.* Noble-metal-free Cu_2S-modified photocatalysts for enhanced photocatalytic hydrogen production by forming nanoscale p-n junction structure. RSC Adv, 2015, 5: 18159–18166
26 Chen Y, Wang L, Lu GM, *et al.* Nanoparticles enwrapped with nanotubes: a unique architecture of CdS/titanate nanotubes for efficient photocatalytic hydrogen production from water. J Mater Chem, 2011, 21: 5134–5141
27 Meng F, Li J, Cushing SK, *et al.* Solar hydrogen generation by nanoscale p-n junction of p-type molybdenum disulfide/n-type nitrogen-doped reduced graphene oxide. J Am Chem Soc, 2013, 135: 10286–10289
28 Manna G, Bose R, Pradhan N. Semiconducting and plasmonic copper phosphide platelets. Angew Chem Int Ed, 2013, 52: 6762–6766
29 Ni S, Ma J, Lv X, *et al.* The fine electrochemical performance of porous Cu_3P/Cu and the high energy density of Cu_3P as anode for Li-ion batteries. J Mater Chem A, 2014, 2: 20506–20509
30 Villevieille C, Robert F, Taberna PL, *et al.* The good reactivity of lithium with nanostructured copper phosphide. J Mater Chem, 2008, 18: 5956–5960
31 Liang Q, Li Z, Yu X, *et al.* Macroscopic 3D porous graphitic carbon nitride monolith for enhanced photocatalytic hydrogen evolution. Adv Mater, 2015, 27: 4634–4639
32 Xiong J, Wang Y, Xue Q, *et al.* Synthesis of highly stable dispersions of nanosized copper particles using L-ascorbic acid. Green Chem, 2011, 13: 900–904
33 Butler MA. Photoelectrolysis and physical properties of the semiconducting electrode WO_2. J Appl Phys, 1977, 48: 1914–1920
34 Zhang G, Lan ZA, Lin L, *et al.* Overall water splitting by Pt/g-C_3N_4 photocatalysts without using sacrificial agents. Chem Sci, 2016, 7: 3062–3066
35 Chen Z, Berciaud S, Nuckolls C, *et al.* Energy transfer from individual semiconductor nanocrystals to graphene. ACS Nano, 2010, 4: 2964–2968
36 Han C, Wu L, Ge L, *et al.* AuPd bimetallic nanoparticles decorated graphitic carbon nitride for highly efficient reduction of water to H_2 under visible light irradiation. Carbon, 2015, 92: 31–40
37 Bi L, Xu D, Zhang L, *et al.* Metal Ni-loaded g-C_3N_4 for enhanced photocatalytic H_2 evolution activity: the change in surface band bending. Phys Chem Chem Phys, 2015, 17: 29899–29905
38 Cao S, Low J, Yu J, *et al.* Polymeric photocatalysts based on graphitic carbon nitride. Adv Mater, 2015, 27: 2150–2176
39 Qin Z, Chen Y, Huang Z, *et al.* Composition-dependent catalytic activities of noble-metal-free NiS/Ni_3S_4 for hydrogen evolution reaction. J Phys Chem C, 2016, 120: 14581–14589
40 Zhang J, Qi L, Ran J, *et al.* Ternary NiS/Zn_x Cd_{1-x}S/reduced graphene oxide nanocomposites for enhanced solar photocatalytic H_2-production activity. Adv Energy Mater, 2014, 4: 1301925
41 Chen J, Shen S, Guo P, *et al.* *In-situ* reduction synthesis of nano-sized Cu_2O particles modifying g-C_3N_4 for enhanced photocatalytic hydrogen production. Appl Catal B-Environ, 2014, 152-153: 335–341
42 Chen Y, Qin Z, Chen T, *et al.* Optimization of $(Cu_2Sn)_xZn_{3(1-x)}S_3$/CdS pn junction photoelectrodes for solar water reduction. RSC Adv, 2016, 6: 58409–58416
43 Kronik L, Shapira Y. Surface photovoltage phenomena: theory, experiment, and applications. Surf Sci Rep, 1999, 37: 1–206

Acknowledgements The authors thank the financial support from the National Natural Science Foundation of China (21606175), the grant support from China Postdoctoral Science Foundation (2014M560768), and China Fundamental Research Funds for the Central Universities (xjj2015041).

Author contributions Chen Y and Qin Z designed the project; Qin Z, Wang M, and Li R performed the experiments; Chen Y and Qin Z wrote the paper. All authors contributed to the general discussion.

Conflict of interest The authors declare no conflict of interest.

Supplementary information Supporting data are available in the online version of the paper.

Zhixiao Qin received his bachelor degree from Xi'an Jiaotong University in 2013. He is currently a PhD student at Xi'an Jiaotong University. His research interests focus on photocatalytic and photoelectrochemical water splitting.

Yubin Chen is an associate professor at Xi'an Jiaotong University. He received his bachelor degree in 2007 and PhD degree in 2013 from Xi'an Jiaotong University. From 2011 to 2012, he studied at Case Western Reserve University as a visiting scholar. His current research interests focus on photocatalysis, water splitting and functional nanomaterials for energy conversion.

新型磷化铜/氮化碳p-n异质结光催化剂的太阳能产氢性能研究

秦知校, 王朦胧, 李锐, 陈玉彬*

摘要 开发高效的异质结光催化剂促进电荷的分离和转移对提高太阳能光催化产氢性能至关重要. 本文采用p型的磷化铜和n型的氮化碳形成p-n结来促进电荷分离和转移, 从而提高光催化产氢性能. 与纯的氮化碳相比, 磷化铜/氮化碳p-n异质结光催化剂的产氢性能提高了95倍, 在420纳米处的量子效率达到2.6%. 我们通过荧光光谱, 表面光电压谱以及电化学测试进一步分析反应机理, 发现显著提高的光催化产氢性能应归因于p-n异质结光催化剂中高效的电荷分离. 本研究表明形成p-n异质结是开发高效光催化剂的一种有效途径.